ACS APPLIED MATERIALS & INTERFACES

Research Article

www.acsami.org

Branch Density-Controlled Synthesis of Hierarchical TiO_2 Nanobelt and Tunable Three-Step Electron Transfer for Enhanced Photocatalytic Property

Debabrata Sarkar[†] and Kalyan Kumar Chattopadhyay*[,†,‡]

[†]School of Material Science & Nanotechnology, and [‡]Thin Film & Nanoscience Laboratory, Department of Physics, Jadavpur University, Kolkata 700 032, India

Supporting Information

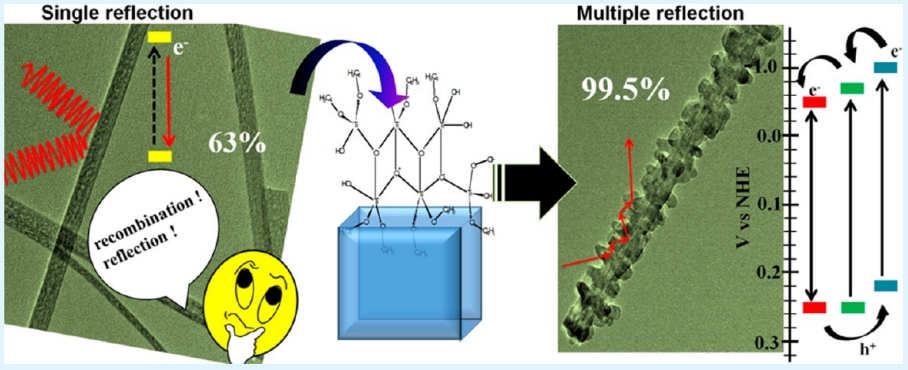

ABSTRACT: The successful adjustment of phase composition and morphology of hierarchical TiO_2 nanobelts, which feature homoepitaxial nanobranches, has been developed via the hydrothermal method and chemical bath deposition technique. Effects of hydrothermal reaction time, titanium butoxide treatment in chemical bath deposition, and calcination temperature are systematically investigated. For the first time, three-step ultrafast electron transfers between the band edges of the engaged phases are realized through the enhanced photocatalytic activity results. Growth mechanism related to branch density control on nanobelt surface under such soft chemical process is discussed in detail on the basis of classical nucleation theory. The current work might provide new insights into the fabrication of one-dimensional homoepitaxial branched TiO_2 nanostructures as high performance photocatalysts and facilitate their application in environmental cleanup.

KEYWORDS: *TiO_2, branched nanobelts, phocatalysis, charge transfer, Raman spectra, nucleation theory*

INTRODUCTION

In advanced materials chemistry, constructing complex nanostructures with controllable morphology and crystallinity is highly important for optimizing their physical and chemical properties.[1,2] In recent years, enormous efforts have been devoted toward the synthesis of inorganic materials with unusual and complex nanoarchitectures due to their exotic properties and wide applications in electronic, optoelectronic, magnetic, and electrochemical nanodevices and as well as in issues such as biomedical, environmental, and energy storage frontiers. Among the above, photocatalysis plays an indispensible role for green civilization.[3,4] To remove toxic ions and organic pollutants from water for a clean and eco-friendly environment, photocatalysis is considered as an environmentally benign method. Among various oxide-based catalysts, titanium dioxide (TiO_2) is proven to be the most suitable and promising candidate for its high physical and chemical stability, nontoxicity, effectivity, high oxidizing power, and cost efficiency.[5,6] The overall photocatalytic reaction involves three major steps: (i) absorption of light by semiconductor to generate electron−hole pairs, (ii) charge separation and migration to the surface of semiconductor, and (iii) surface reactions for water reduction or oxidation. Subject to these major processes, photocatalytic activity is found to be majorly dependent on size, shape, surface area, morphology, dimensionality, crystallinity, and the phases of the catalysts.[7,8]

One-dimensional (1D) TiO_2 nanostructures such as nanorods, nanobelts, or nanowires are extensively studied due to their potential application as photocatalysts, solar cells, gas sensors, and lithium-ion batteries.[9−12] The photocatalytic activity of 1D TiO_2 nanobelts or nanowires is relatively low due to the presence of fewer active surface sites and high recombination of photogenerated electron−hole pairs of the single phase nanostructure.[13−15] To enhance the active surface site and reduce the charge recombination, new nanostructures combined with branches for large specific surface area are

Received: January 10, 2014
Accepted: May 23, 2014
Published: May 23, 2014

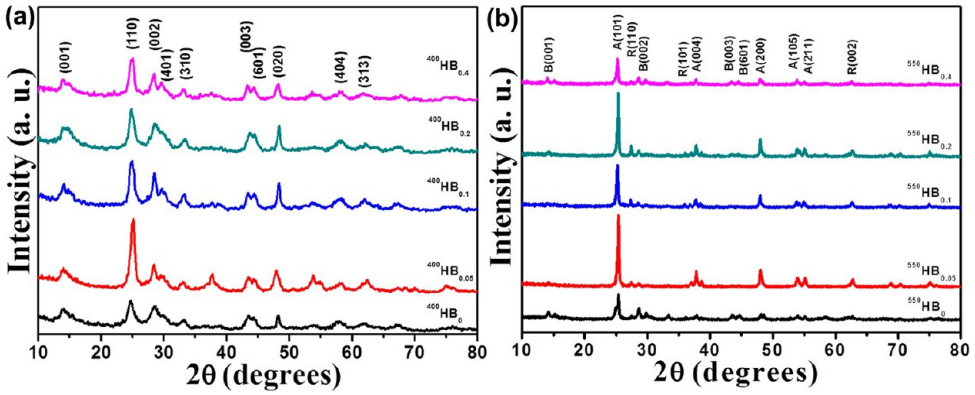

Figure 1. XRD patterns of (a) single phase bare and branched TiO_2 nanobelts annealed at 400 °C, and (b) mixed phase bare and branched TiO_2 nanobelts annealed at 550 °C.

desirable. Over the past decades, much effort was devoted to the development of different techniques for designing and fabrication of hierarchical nanostructures with well-controlled morphology and controlable crystallinity such as sol−gel method, hydrothermal/solvothermal method, chemical vapor deposition, physical vapor deposition, electrochemical deposition, etc.[16−19] The formation of hierarchical structure is generally considered to be a self-assembly process. Mixed-phase one-dimensional TiO_2 nanobelts with nanobranches would lead to superior photocatalytic abilities as the electron−hole separation at the interface arises from the band alignment, and multiple reflections and scattering of UV light. Most of the mentioned methods have poor control over the morphology and density of the branches, which affect their properties. To take advantage of such hierarchical nanobranches for superior photocatalysis application, one must control them precisely at the stage of growth. To date, it is even more challenging to control the size, morphology, and crystal phase of hierarchical TiO_2 nanostructures in a predictable manner. Among other growth deposition techniques, the "chemical bath deposition" approach is quite appropriate for the synthesis of second-order branched structures on primary nanostructures due to available excellent control over the structure, morphology, and dimensions of the obtained branches.[20−28] Also, in chemical bath deposition, the solubility of solutes can easily change, and a small degree of supersaturation of the solution causes the heterogeneous nucleation.

To handle the aforementioned problems, we introduce a facial and effective approach, incorporating solvothermal with a chemical bath deposition process to synthesize branched TiO_2 nanostructure that is expected to greatly improve the degradation rate of methyl orange solution. The morphology, density of the branches, and phases of the branched nanobelts can be facilely controlled. The influences of precursor concentration on the growth of branches and the growth mechanism of these hierarchical branch nanobelts are also discussed in detail. To the best of our knowledge, the current work is the first report regarding TiO_2(B)/anatase/rutile mixed phase branch nanobelts synthesis. For different branch densities, suitable growth mechanisms of nanocrystal nucleation and growth are also proposed. Finally, the photocatalytic activities of synthesized nanobelts are assessed for methyl orange as a model pollutant, and the degradation kinetics are evaluated in detail.

EXPERIMENTAL DETAILS

Materials Preparation. *Preparation of Titanate Nanobelts.* TiO_2 nanobelts were prepared by the hydrothermal method. In this method, the sizes of the nanobelts can be controlled by varying the reaction temperatures and reaction time. In a typical reaction, 0.4 g of anatase TiO_2 (Sigma-Aldrich) was first dispersed in 10 mL of 10 M NaOH aqueous solution. After the solution was stirred for 15 min, 10 mL of ethanol was added to the mixture solution. After being stirred for 30 min, the mixtures were heated at 200 °C for 6−72 h in a 100 mL Teflon-lined stainless-steel autoclave and then cooled to room temperature naturally. Next, the prepared cake-like sodium titanate nanobelts were immersed in a mixture of 100 mL of DI and 8 mL of HCl (35% by weight) for 10 h for transformation of sodium titanate nanobelts to hydrogen titanate nanobelts. The white hydrogen titanate nanobelt was filtered and washed thoroughly with deionized water until pH ≈ 7 was reached.

Preparation of Branched TiO_2 Nanobelts. The titanate nanobelts assembled by branches were prepared by chemical bath deposition. All syntheses were carried out in a 100 mL round-bottom flask equipped with a condenser, which was heated in an oil bath to a temperature of 60 °C. 0.05 g of prepared titanate nanobelts was placed into 50 mL of titanium butoxide ($Ti(OC_4H_9)_4$) solution, which was prepared by mixing 50 mL of DI water, 0.4 mL of concentrated HCl (38% by weight), and $Ti(OC_4H_9)_4$. Dilute acidic titanium butoxide was used to grow TiO_2 nucleus at 60 °C under stirring for 6 h. The TiO_2 nucleus was controlled by varying the $Ti(OC_4H_9)_4$ amount as 0.05, 0.1, 0.2, and 0.4 mL. Finally, the hierarchical nanobelts consisting of long trunks and very short branches were washed and dried in air. After that, further annealing in air at 400 and 550 °C for 2 h is required for TiO_2 nanobelt with branched structures with different phases.

Materials Characterization. The crystal structures of products were examined by X-ray difraction (XRD, Rigaku-Ultima-III). The morphologies of the nanostructures were characterized by scanning electron microscopy (FESEM, Hitachi S4800) and high-resolution transmission electron microscopy (TEM, JEOL 2010) with an accelerating voltage of 200 kV. The chemical composition and chemical status were analyzed with an energy dispersive X-ray (EDS, Thermo scientific, Ultra dry, attached with FESEM) and X-ray photoelectron spectroscopy (XPS, HSA-3500, SPECS, Germany). UV−vis of the samples was recorded on a UV−vis spectrophotometer (UV-2550, Shimadzu) with an integrating sphere attachment. The Raman spectra were carried out with the WITec alpha 300RS system. The time-resolved fluorescence spectra were measured at room temperature by using nanosecond diode excitation source at 350 nm (IBH nanoLED-03) and TBX-04 as a detector.

Photodegradation Reaction. Photocatalytic activity of the synthesized branched TiO_2 nanobelts was carried out in a photoreactor, which was designed with an internal 40 W UV tube (Phillips) with a maximum emission at 254.6 nm. The photodegradation of methyl orange dye (MO, $C_{14}H_{14}N_3$ NaO_3S), a common target known to be carcinogenic and mutagenic, was used to study the photocatalytic

properties. For each measurement, 20 mg of the sample was dispersed within 40 mL of dye solution with a concentration of 10^{-5} M in a 100 mL quartz beaker. Before the photocatalytic activity test, the suspension was continuously stirred in the dark without irradiation for 30 min to establish the adsorption/desorption equilibrium of the dye on the nanobelt. At a given time interval, 3 mL of suspension was taken out and analyzed after removal of catalyst particles by filtration. The quantity of MO in solution was determined by the absorbance intensity at 268 nm (main absorption peak of MO) using a UV−vis spectrometer.

RESULTS AND DISCUSSION

X-ray Diffraction (XRD). The crystal structures and phase of the synthesized materials are characterized by X-ray diffraction (XRD), as shown in Figure 1. The XRD patterns of prepared sodium titanate ($Na_2Ti_nO_{2n+1}$) and hydrogen titanate nanobelts ($H_2Ti_nO_{2n+1}$) are shown in Supporting Information Figure S1, which shows the first crystalline sodium titanate nanobelts obtained by the hydrothermal method (PCPDFWIN no. 72-0148 and PCPDFWIN no. 80-0467), and after ion exchange crystalline branched hydrogen titanate is obtained (PCPDFWIN no. 41-0192 and PCPDFWIN no. 44-0131). The crystal structure influences the photocatalytic properties, and it has been shown that single phase-based TiO_2 catalyst will have lower activity than mixed phase catalyst.[29] It was observed that a pure nanocrystalline titania consisting of TiO_2(B) and a mixture of TiO_2(B)/anatase/rutile were obtained with controlled variation in calcination temperature. The XRD pattern of hierarchical TiO_2(B) nanobelt after calcination of hierarchical hydrogen titanate nanobelt at 400 °C for 2 h is depicted in Figure 1a. The formation of TiO_2(B) nanobelts assembled with homoepitaxial TiO_2 nanobranches belongs to the *C*2/*m* space group (PCPDFWIN no. 46-1237). When the calcination temperature reaches 550 °C, the XRD of the corresponding sample shows a mixed phase of anatase, rutile, and TiO_2(B). It can be observed from Figure 1b that anatase (tetragonal) is the main phase having three major diffraction peaks at 2θ values of 25.3°, 37.79°, and 48.04° (PCPDFWIN no. 78-2486) with two shoulders of rutile at 27.4° and 36° (PCPDFWIN no. 86-0147) and four weak shoulders of TiO_2(B) at 14.19°, 28.61°, 43.51°, and 44.50°. Mean crystallite sizes of TiO_2(B) and anatase phase were calculated from the line-broadening of XRD diffraction peaks at 24.9° and 25.3°, respectively. However, when the temperature was increased further to 700 °C, the crystallinity of the anatase phase increases significantly. Supporting Information Figure S2 shows that the weak peak of TiO_2(B) at 14.19°, 28.61° disappeared. That means the TiO_2(B) was slowly transformed into anatase phase.

Therefore, the phase composition in the samples was controlled carefully by annealing time, and thereby the ratio of anatase, rutile, and TiO_2(B) was changed dramatically. With increasing calcination temperature, the peak intensity increases significantly. The average crystallite sizes of TiO_2(B) and TiO_2(B)/anatase/rutile hierarchical nanobelts were calculated using Scherrer's equation for the main diffraction peak via

$$D = \frac{K\lambda}{\beta \cos\theta} \quad (1)$$

where D is the average crystallite size obtained in angstroms (Å) and K is the shape factor taken to be 0.9, λ is the wavelength of X-ray radiation (Cu Kα = 1.5406 Å), β is the full width at half-maximum height in radians, and θ is the corresponding Bragg angle of the XRD peak in radians. By increasing calcination temperature from 400 to 700 °C, the crystallite size of TiO_2(B) and anatase monotonically increased from 8.2 to 36.7 nm. The details of the experimental parameters, crystallite size, and crystal structure phase are listed in Table 1.

Table 1. Details of the Experimental Parameters, Crystallite Size, and Crystal Phase

	experimental parameters			
sample	$Ti(OC_4H_9)_4$ treatment (mL)	calcination temp (°C)	crystal phase	crystal size (in nm)
TiO_2 nanobelts				8.21
	0.05			10.9
hierarchical TiO_2	0.1			9.35
nanobelts ($^{400}HB_x$)	0.2	400	TiO_2(B)	9.68
	0.4			9.57
TiO_2 nanobelts				12.52
	0.05			30.16
hierarchical TiO_2	0.1			29.27
nanobelts ($^{550}HB_x$)	0.2	550	TiO_2(B)/anatase	36.79
	0.4		/rutile	23.44
TiO_2 nanobelts				42.41
	0.05			35.57
hierarchical TiO_2	0.1			41.80
nanobelts ($^{700}HB_x$)	0.2	700	anatase/rutile	43.59
	0.4			38.74

Morphology and Structure. The morphology and structure of the smooth and hierarchical nanobelts are first characterized by field emission scanning electron microscopy (FESEM) and transmission electron microscopy (TEM). The morphologies of the hydrogen titanate nanobelts synthesized by hydrothermal method at 200 °C with different reaction times are displayed in Supporting Information Figure S3. Supporting Information Figure S3a, c, and d shows the sample synthesized after 5, 12, and 72 h of hydrothermal reaction, respectively, exhibiting bundles of nanobelt with short length and large diameters. Supporting Information Figure S3b shows a typical FESEM image of the nanobelts after 8 h of hydrothermal reaction; these nanobelts exhibited comparatively smooth surface, long length, and small uniform diameters over their entire lengths. Up to now many researchers[30−34] found TiO_2 nanobelt, which was formed after the calcinations of hydrogen titanate nanobelts, but in this work first we focus to tune the length, diameter, morphology, and phases of the synthesized nanobelts. Both are important for photocatalysis applications. To demonstrate the advantages of homoepitaxial nanobranches with different phases in photocatalytic applications, we compared the catalyst morphology as shown in Figure 2. Figure 2a and b displays titanate nanobelts of length ranging up to several tens (30−50) of micrometers. As shown in the high magnification FESEM images (Figure 2c and d), the nanobelts have a smooth surface with a diameter in the range of 25−60 nm. Figure 2e−p illustrates FESEM images of

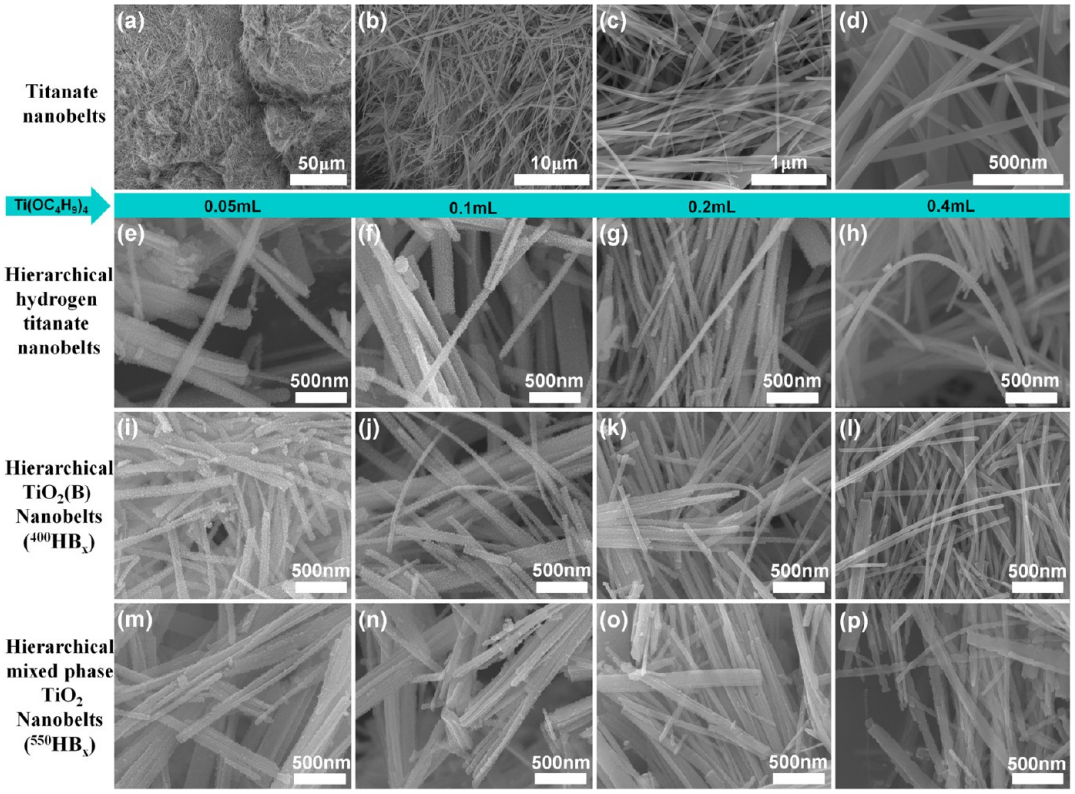

Figure 2. FESEM images of as-prepared samples show the evolution of TiO_2 hierarchical structures with different experimental conditions. (a–d) Bare TiO_2 nanobelt, (e–h) hierarchical hydrogen titanate nanobelts, (i–l) hierarchical TiO_2(B) nanobelts annealed at 400 °C, and (m–p) hierarchical mixed phase TiO_2 nanobelts annealed at 550 °C.

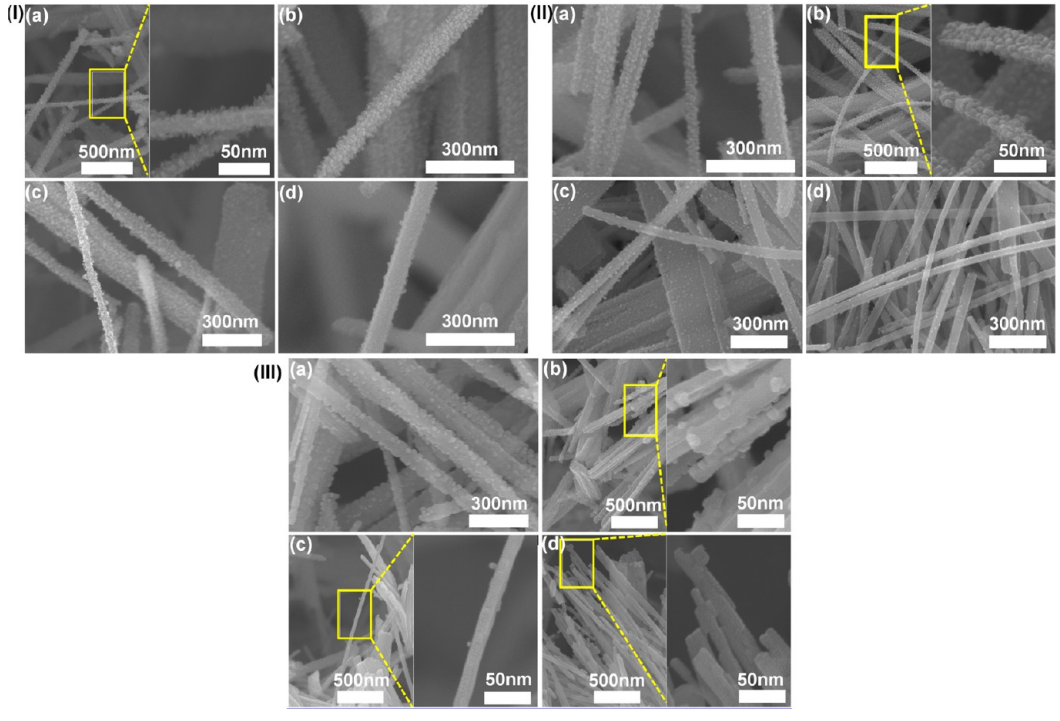

Figure 3. High magnification FESEM images of hierarchical branched (I) hydrogen titanate nanobelts, (II) TiO_2(B), and (III) TiO_2 (mixed phase; TiO_2(B)/anatase/rutile) grown in chemical bath deposition in HCl solutions containing different amounts of titanium butoxide: (a) 0.05 mL, (b) 0.1 mL, (c) 0.2 mL, and (d) 0.4 mL.

hierarchical TiO_2 nanobelts where the branches were synthesized by a simple chemical bath deposition method. The hierarchical hydrogen titanate nanobelts consist of many short nanorod branches (Figure 2e–h). Figure 2i–l shows branched nanobelts heated at 400 °C with different titanium butoxide treatment, and Figure 2m–p shows branched

dx.doi.org/10.1021/am502379q | ACS Appl. Mater. Interfaces 2014, 6, 10044–10059

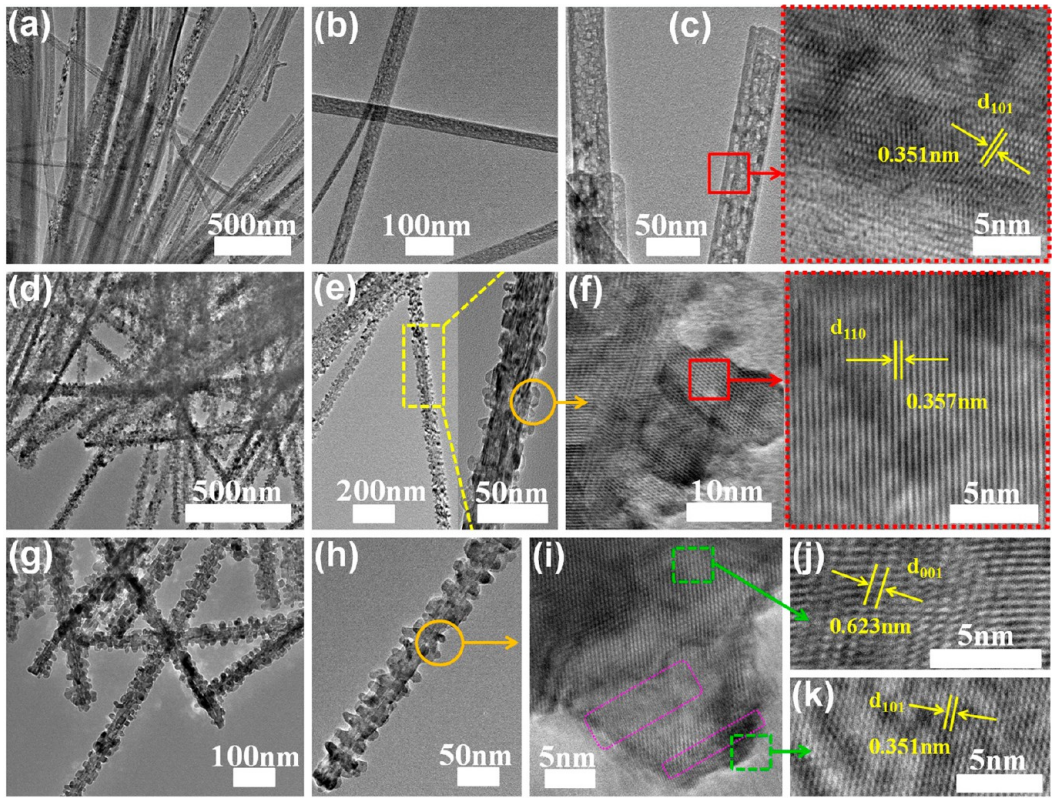

Figure 4. Typical TEM and HRTEM images of TiO_2 nanostructures: (a–c) bare TiO_2 nanobelts; (d–f) TiO_2(B) branched nanobelts; and (g–k) mixed phase nanobelt with branch structures.

nanobelts heated at 550 °C with different titanium butoxide treatment, which clearly indicates with increasing calcination temperature the nanobelt morphologies have no obvious change. Yet the morphology of the branches, such as diameter, length, and density, was well controlled by varying the synthesis conditions. As the chemical reaction proceeded in chemical bath deposition, however, new features started to evolve on the smooth surface of the nanobelts. The resulting morphology was dependent on the amount of titanium butoxide in $Ti(OC_4H_9)_4$ solution. We can see that the hierarchical nanostructures were formed on the surface of the nanobelts. Figure 2i–p shows the density of the nanobranches increases to 0.1 mL of $Ti(OC_4H_9)_4$ treatment that leads to form nanobranches on the nanobelt surface for further increase in surface area. When the amount of $Ti(OC_4H_9)_4$ was 0.2 mL, the nanobelts were partially coated with nanobranches. Further increasing the $Ti(OC_4H_9)_4$ amount to 0.4 mL led to much less coverage of nanobranches. The HCl acid effect on the nanobelts examined in the same experimental condition without $Ti(OC_4H_9)_4$ is shown in Supporting Information Figure S4a. Also, we examined nanobelts with $Ti(OC_4H_9)_4$ but without the acid treatment, which is shown in Supporting Information Figure S4b, and we get nanobelts with particle agglomeration. Supporting Information Figure S4 illustrates that the nanobelts have smooth surfaces, which are similar to nanobelts without the acid treatment. So we conclude that without $Ti(OC_4H_9)_4$ or HCl in chemical bath deposition, the morphology of the nanobelts does not change any more. When the calcination temperature increases to 700 °C, the hierarchical branches nanobelt morphology was completely destroyed, and only small nanorods with sizes of 100 nm to 5 μm are observed (Figure S5, Supporting Information). Examination of individual hierarchical nanobelts with different branch densities and different phases is shown in Figure 3. High magnification FESEM images of the as-prepared hierarchical hydrogen titanate nanobelt are shown in Figure 3I. The high magnification FESEM images (Figure 3II and III) are provided to understand the morphology change of the as-prepared hierarchical TiO_2 nanobelt assembled with homoepitaxial nanobranches at different amounts of $Ti(OC_4H_9)_4$ treatment. After chemical bath deposition, the nanobelts are covered with nanobranches having length ~20 nm and diameater ~7–10 nm. When the calcination temperature reaches 550 °C, the diameter of the branches increases due to grain growth of the nanograins. The detailed growth mechanism is described in our previous work.[35] As the amount of $Ti(OC_4H_9)_4$ in the solution increased, the density of the nanobranch array also increased (parts a,b of Figure 3I–III, respectively). Meanwhile, with a further increase in the $Ti(OC_4H_9)_4$ amount to 0.2 and 0.4 mL, the TiO_2 nanobranch array density gradually decreased (parts c,d of Figures 6, 7, and 8, respectively). To optimize both nanobranch density and surface area for photocatalytic activity, the acidic medium chemical bath deposition was selected for all of the experiments in this Article. The chemical composition of these nanobelts was determined from the energy-dispersed spectrum. The observation of two peaks for Ti and O indicates that the nanobelts are pure TiO_2, and the atomic ratio of Ti to O was found close to 1:2 (Supporting Information Figure S6a). Supporting Information Figure S6b corresponds to the EDX elemental mapping images of Ti and O.

The details of microstructures of the samples were further investigated by high-resolution transmission electron microscopy (HRTEM), and the corresponding images are presented in Figure 4. Figure 4a–c shows three TEM images of TiO_2

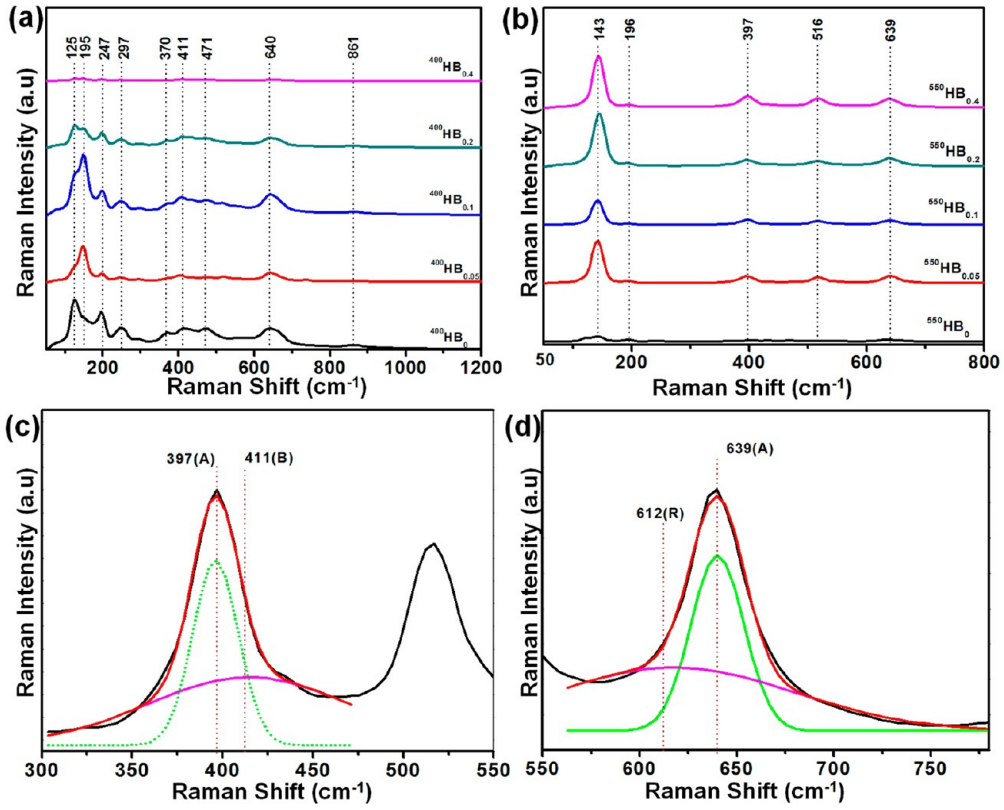

Figure 5. Raman spectra of the bare and branch (a) TiO_2(B) nanobelts, and (b–d) mixed phase TiO_2 nanobelts.

nanobelts, which indicate nanobelts are well-dispersed and flexible with smooth surface. As shown, the diameter is about 40 nm, and the length is of the order of micrometers. This value is different from crystallite size, which is calculated from XRD. Our grown nanobelt samples were not single crystalline in nature, but polycrystalline. The Debye–Scherrer equation actually provides crystallite size or length of coherence of the crystal planes perpendicular to the direction of the X-ray beam and not the exact particle size. As the belts were polycrystalline, hence composing crystallites had random orientation. The HRTEM image clearly shows that the nanobelts have a layered structure (Figure 4c) with interplanar distances of d_{101} = 0.351 nm. The clear lattice fringes of the nanobelts reveal that the growth front of the TiO_2 nanobelt is the (101) planes. The prepared titanate nanobelts could be further converted into branched nanobelts with additional chemical bath deposition shown in Figure 4d–k. These hierarchical nanobelts are composed of smaller branches with width of about 8 nm and length of about 15 nm (Supporting Information Figure S7). It can be clearly observed that nanobranches grow on the surface of the TiO_2 nanobelts. Figure 4d–f displays TEM and HRTEM images of hierarchical nanobelts calcined at 400 °C for 2 h. The average diameter of the branched nanobelts is approximately 40 nm (Figure 4e). The *d*-spacing of d_{110} = 0.357 nm corresponds well with that of the (110) plane of TiO_2(B). We get the mixed phase nanostructure by changing the calcination temperature from 400 to 550 °C. Figure 4g–k shows a TEM image of branched TiO_2(B)/anatase/rutile nanobelts and its corresponding HRTEM image, respectively. A careful observation of Figure 4i illustrates that there is a coexistence of two sets of lattice, and a continuity of lattice fringes between the interfaces of these two phases is shown by pink rectangles. The lattice fringes, taken from the region labeled by green squares marked as in Figure 4i, are depicted in Figure 4j and k, which reveal that the nanostructures are highly crystalline. Two sets of lattice fringes with interplanar spacing of d_{001} = 0.623 nm and d_{101} = 0.351 nm clearly indicated in the magnified HRTEM image are attributed to (001) plane of TiO_2(B) and (101) plane of the anatase nanocrystal, respectively, that form a heterojunction interface. Supporting Information Figure S7 shows the branches were formed on the primary nanobelts perpendicular to the propagating axis of primary TiO_2 nanobelts. Such a hierarchical branch structure provides a large external surface area, which has a high photocatalytic activity. Therefore, suitable hydrothermal and controlled chemical bath deposition are important for optimimal density and quality of TiO_2 branch nanobelts.

Raman Spectra. Raman spectroscopy is an ideal characterization method to discriminate between the different crystalline morphologies of TiO_2 due to their distinct vibrational modes. Figure 5a shows the Raman spectra of bare and branched TiO_2 nanobelt calcined at 400 °C. The Raman spectra of the five samples ($^{400}HB_x$) are depicted between 50 and 1200 cm^{-1}, and they are characteristic of the TiO_2(B) variety with nine scattering diffusion active modes located at 125, 195, 247, 297, 370, 411, 471, 640, and 861 cm^{-1}. The band positions for the TiO_2(B) phase are in excellent agreement with published data.[36,37] This result is well accordant with that of XRD (Figure 1). Figure 5a also shows that the intensity of the Raman peak for sample $^{400}HB_{0.4}$ is minimum (magnified spectra are shown in Supporting Information Figure S8), which substantiates that the Raman modes are not dependent upon crystallinity of the samples. Phase changes due to calcination at 550 °C were fully investigated by Raman spectroscopy. According to the symmetry group analysis, anatase and rutile structures have three acoustic modes and 15 optical modes. Among the optical

modes, for anatase the irreducible representations are $1A_{1g} + 1A_{2u} + 2B_{1g} + 1B_{2u} + 3E_g + 2E_u$. The vibration of B_{2u} is inactive in both the infrared and the Raman spectra. For rutile the irreducible representations are $1A_{1g} + 1A_{2g} + 1A_{2u} + 1B_{1g} + 2B_{1u} + 1B_{2g} + E_g + 3E_u$. Here, $A_{2g} + 2B_{1u}$ are neither Raman active nor infrared active. Representations with the subscript "u" are IR-active, while representations with the subscript "g" are Raman active and E is degenerate. For samples $^{550}HB_x$, the characteristic bands due to TiO_2(B) phase almost disappear, and five new strong bands at 143, 196, 397, 516, and 639 cm^{-1} are observed (Figure 5b). All of these bands are assigned to the anatase phase.[38] The magnified Raman spectra are illustrated in Supporting Information Figure S9. Except for the anatase band discussed above, only one nonoverlapping weak Raman signature of TiO_2(B) obtained at 244 cm^{-1} indeed proves the existence of TiO_2(B) phase. The XRD pattern shows that the samples are of mixed phase of anatase, rutile, and TiO_2(B). The peak position for rutile Raman active B_{1g} mode centered at 143 cm^{-1} may overlap with anatase E_g mode (144 cm^{-1}). It is important to deconvolute the superimposed broad peaks at 397 and 639 cm^{-1}, because this allows a better identification of the individual bands. The as-recorded spectra were fitted and deconvoluted by using Gaussian function and Gaussian deconvolution methods, which are shown in Figure 5c. It can be observed from Figure 5c and d that there are two bands near 397, 411 cm^{-1} and 612, 639 cm^{-1}. The peak at 411 cm^{-1} assigned to TiO_2(B) and at 612 cm^{-1} indicates rutile A_{1g} mode of TiO_2.[36,38] The observed Raman modes for all samples are summarized in Table 2, and they are in good agreement with reported literature data.[39]

Table 2. Vibration Frequencies and Mode Assignments of Observed Raman Bands for Samples $^{400}HB_x$ and $^{550}HB_x$

sample	phase	Raman modes (cm^{-1})	mode assignment
		125	B_g
		195	B_g
		247	B_g
		297	A_g
$^{400}HB_x$	TiO_2(B)	370	A_g
		411	A_g
		471	A_g
		640	B_g
		861	A_g
$^{550}HB_x$		143	E_g
		196	E_g
	anatase	397	B_{1g}
		516	$A_{1g} + B_{1g}$
		639	E_g
	rutile	612	A_{1g}
		244	B_g
	TiO_2(B)	411	A_g

Growth Mechanism. On the basis of the above analysis, we propose a simple three-step growth process. The preparation of TiO_2 nanobelt assembled with homoepitaxial nanobranches is shown in Scheme 1. (a) Hydrogen titanate nanobelt ($N_2Ti_nO_{2n+1}$): First, bulk anatase TiO_2 powder reacts with the NaOH aqueous solution and forms a layer-like lamellar product. At 200 °C in hydrothermal condition, this reaction is very fast and produces a large amount of titanate particles, and these particles grow very quickly along a certain plane, forming single layer titanate nanobelts ($Na_2Ti_nO_{2n+1}$). Now these single layer titanate nanobelts superposed to each other to form detectable sodium titanate nanobelts, which are in HCl solution allowing ion exchange from Na^+ ions of sodium titanate by H^+ to form hydrogen titanate ($H_2Ti_nO_{2n+1}$).

$$3TiO_2 + 2NaOH \xrightarrow{\text{hydrothermal}} Na_2Ti_nO_{2n+1} \quad (2)$$

$$Na_2Ti_nO_{2n+1} + 2HCl \xrightarrow{\text{ion exchange}} H_2Ti_nO_{2n+1} + 2NaCl \quad (3)$$

These sodium titanate nanobelts are made up of TiO_6 octahedra that share edges to form two-dimensional sheets. These sheets are held together and electrostatically stabilized with Na^+ and OH^- between the layers. After the ion exchange, the TiO_6 octahedra layers remain unchanged, but the Na^+ ions are replaced with H^+ ions as shown in the crystal structure in Scheme 1. (b) Hierarchical TiO_2 nanobelt: In this step, through hydrolyzation of $Ti(OBu)_4$ under acidic condition, titanate nuclei were formed and attached to the nanobelt surface. It is noted from Supporting Information Figure S4 that the seed layer is mandatory for hierarchical structure because no secondary growth was observed when this step was omitted. With prolonging the reaction time, branches were formed due to each nucleus growth in the direction perpendicular to the nanobelt surface. Here, TiO_2 branches were formed on the titanate nanobelt surface by heterogeneous nucleation mechanism due to a lower free energy as compared to homogeneous nucleation. In the last step, the hydrogen titanate nanobelt assembled with nanobranches transforms into hierarchical TiO_2 nanobelts by thermal annealing.

$$H_2Ti_nO_{2n+1} \xrightarrow{\text{annealing } 400\,^\circ C} TiO_2(B) \quad (4)$$

$$H_2Ti_nO_{2n+1} \xrightarrow{\text{annealing } 550\,^\circ C} TiO_2(B)/\text{anatase/rutile} \quad (5)$$

To explain the effect of the $Ti(OC_4H_9)_4$, a possible mechanism based on the type of nucleation and growth can be assumed for the formation of different nanobranch densities on the TiO_2 belts. In chemical bath deposition, Ti−O−Ti oxo species are formed by hydrolysis of titanium butoxide, which is shown in Figure 6. The growth of the Ti−O−Ti network results in amorphous titania nuclei. According to the classical nucleation theory, the equation for the free energy change (ΔG) due to nucleation of spherical nucleus with radius r from the solution with supersaturation S is described by

$$\Delta G = \frac{4}{3}\Pi r^3 \Delta G_v + 4\Pi r^2 \gamma_{sl} \quad (6)$$

where ΔG_v is the change of Gibb's free energy per unit volume solute transforming from solution to crystallite, and γ_{sl} is the surface free energy per unit area of the solid−liquid interface. The expression of ΔG_v is given below:

$$\Delta G_v = -\frac{kT}{\Omega} \ln \frac{C}{C_0} = -\frac{kT}{\Omega} \ln(1 + S) \quad (7)$$

where Ω is atomic volume, C is the concentration of solute in the solution, and C_0 is the concentration of solute at equilibrium. In the change of the Gibbs free energy, there exists a critical size ($r = r_c = -(2\gamma_{sl})/(\Delta G_v)$) given by maximum ΔG. The nucleus with smaller radius ($<r_c$) is unstable due to the increase of the Gibbs free energy. Thus, the smallest cluster (prenucleation molecular assemblies) in solution typically dissolves. As size increases, total free energy goes through a

Scheme 1. Illustration of the Growth Mechanisms of (a) Nanobelt and (B) Branch Nanobelt

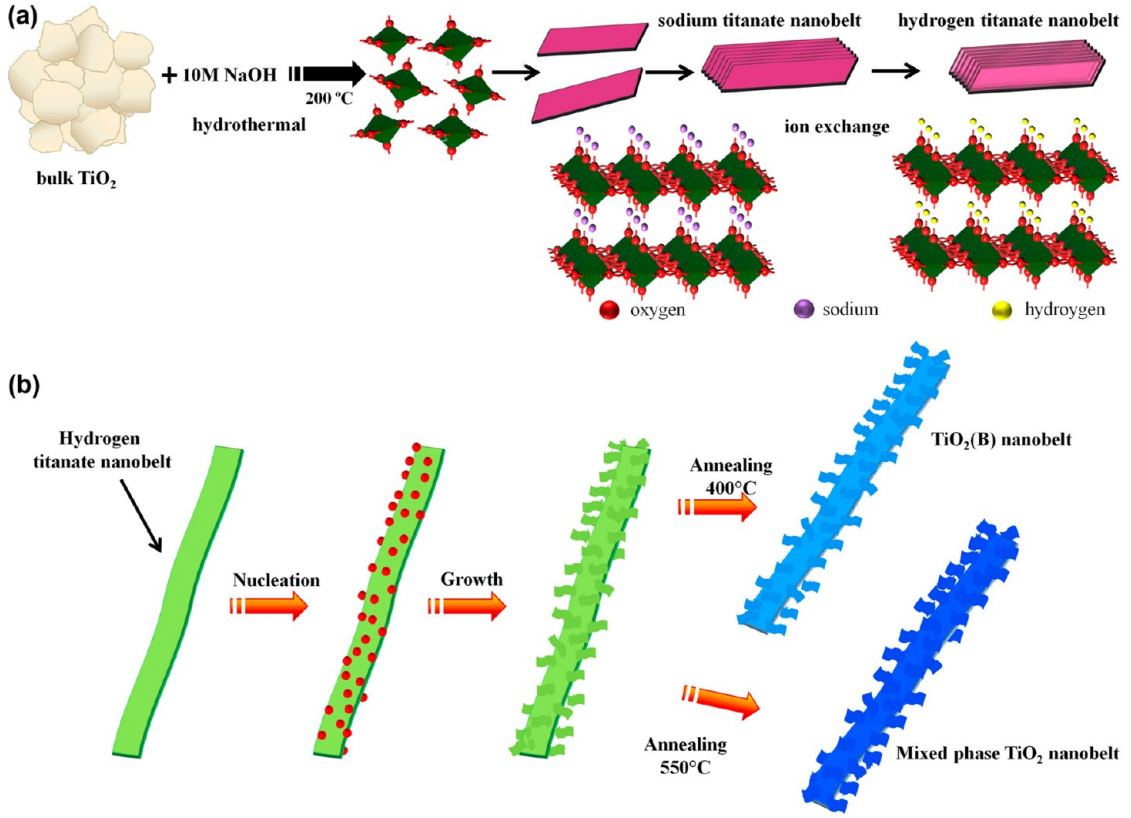

maximum (ΔG_{crit}) at r_c, above which the total free energy decreases continuously and growth becomes energetically favorable, resulting in the formation of crystal nuclei.[40] The height of the energy barrier (ΔG_{crit}), which is the free energy necessary to form a stable nucleus, can be written as[41]

$$\Delta G_{crit} = -\frac{16\Pi\gamma_{sl}^3}{[3(\Delta G_v)^2]} = -\frac{16\Pi\gamma_{sl}^3\Omega^2}{[3(kT \ln S)^2]} \quad (8)$$

Generally, two kinds of nucleation are involved in the precipitation process, homogeneous nucleation and heterogeneous nucleation. Equation 8 is the expression for homogeneous nucleation. Here, heterogeneous nucleation involves the surface of the nanobelt on which the nucleation occurs. If θ is the angle of contact between the nucleus deposit and the nanobelt solid surface, then from Figure 6c it can be written as

$$\gamma_{sl} = \gamma_{sn} + \gamma_{nl} \cos\theta \quad (9)$$

where γ_{sl}, γ_{sn}, and γ_{nl} refer to the surface energies of the solution−solid surface, nucleus−solid interface, and nucleus−solution interface, respectively. Substituting eq 9 in eq 6, we get the expression of ΔG_{crit} as

$$\Delta G_{crit} = -\frac{16\Pi\gamma_{ln}^3\Omega^2}{[3(kT \ln S)^2]}\left[\frac{(2 + \cos\theta)(1 - \cos\theta)^2}{4}\right] \quad (10)$$

If $f(\theta) = ((2 + \cos\theta)(1 - \cos\theta)^2)/4$, then it can be written as

$$[\Delta G_{crit}]_{het} = [\Delta G_{crit}]_{hom} f(\theta) \quad (11)$$

As θ varies from 0 to π, $f(\theta)$ varies from 0 to 1, thus $[\Delta G_{crit}]_{het} < [\Delta G_{crit}]_{hom}$. According to this nucleation theory, most formed monomers are consumed by the growth of heterogeneous nucleation rather than by the formation of homogeneous nucleation. Titanium(IV)butoxide is a bulky molecule with a high molecular weight. So titanium(IV)butoxide has a high supersaturation level (S) even at very low concentration (0.05−0.1 mL per 50 mL of solute), giving maximum nucleation. In this work, at 0.05 and 0.1 mL of $Ti(OC_4H_9)_4$, the produced titanate nucleus nucleated onto the nanobelt surface, and only heterogeneous nucleation occurred in the CBD experiment. Consequently, the finding that after CBD experiment the filtrate solution was clear indicates no homogeneous nucleation occurred at these stages of the reaction. It should be noted that dense nanobranches are observed for 0.05 and 0.1 mL of $Ti(OC_4H_9)_4$. Equations 7 and 10 give that with increasing precursor concentration, degree of supersaturation (S) increases and ΔG_{crit} decreases. As a result, large numbers of nuclei are formed on the nanobelt surface and branch density increases. When we increase the precursor concentration taking 0.2 and 0.4 mL of $Ti(OC_4H_9)_4$, more Ti−O−Ti oxo species produced in the solution lead to a high degree of supersaturation. We observed that after filtration the filtrate solution became cloudy (Supporting Information Figure S10), which suggests that not only heterogeneous but also homogeneous nucleation reactions took place in the solution. Equations 7 and 9 suggest that with increasing precursor concentration, degree of supersaturation also increases. It is known that a higher degree of supersaturation can facilitate the homogeneous nucleation in a solution.[42] In this case, maximum numbers of nuclei are nucleated in the solution as a homogeneous nucleation, and less numbers of nuclei are nucleated onto the nanobelt surface. That is why the density of the nanobranch decreases for 0.2 and 0.4 mL of $Ti(OC_4H_9)_4$ samples.

dx.doi.org/10.1021/am502379q | ACS Appl. Mater. Interfaces 2014, 6, 10044−10059

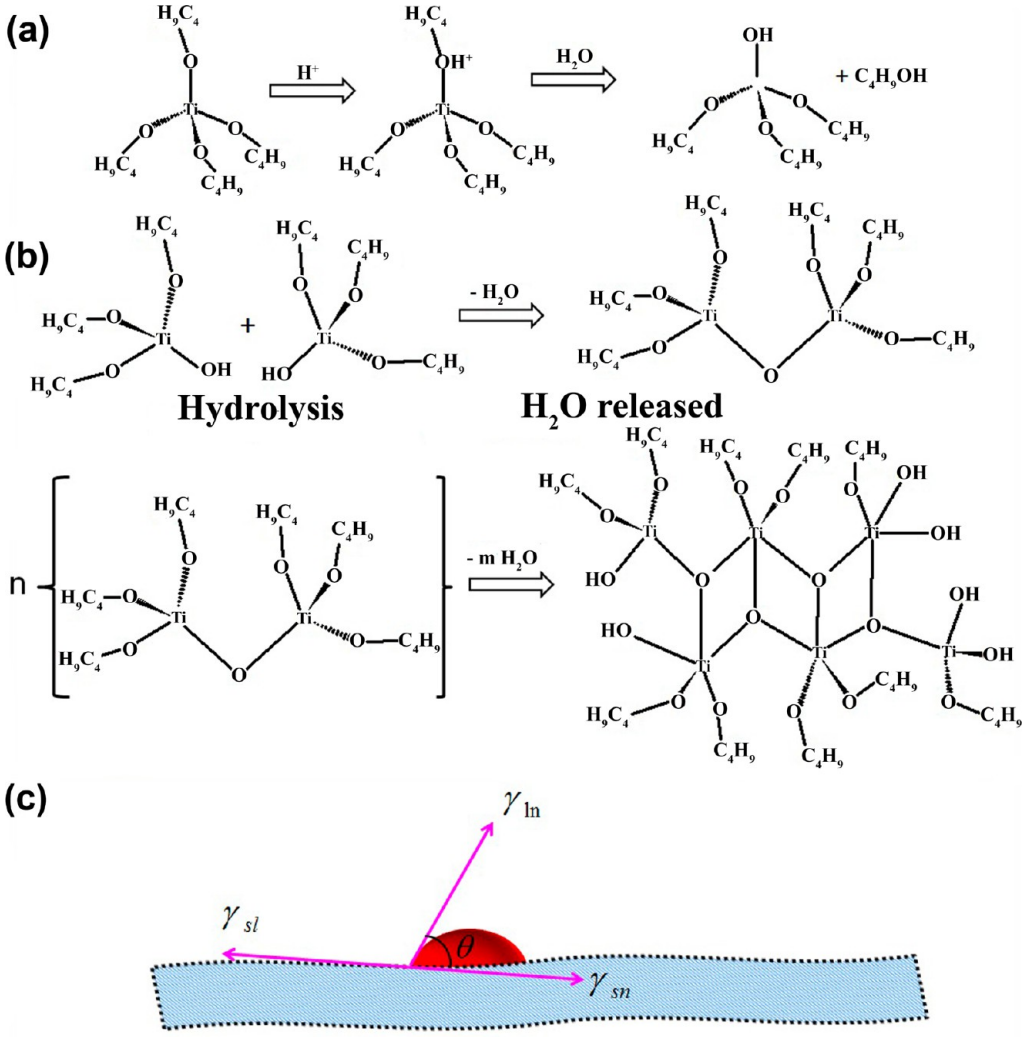

Figure 6. (a,b) Proposed steps for the formation of Ti−O−Ti oxo species, and (c) nucleation on the nanobelt surface and solvent interface.

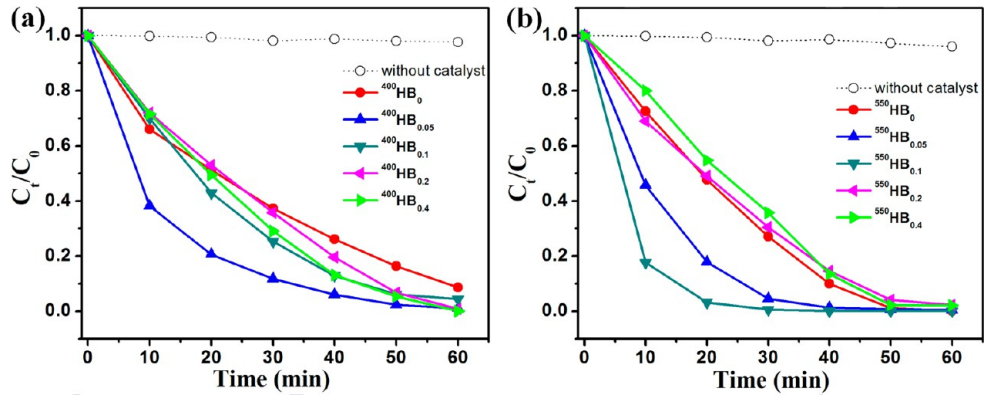

Figure 7. Photocatalysis degradation profiles of methyl orange under UV light irradiation: (a) $^{400}HB_x$ and (b) $^{550}HB_x$.

Photocatalytic Properties. A series of branch structures were synthesized to examine the dependence of photocatalytic performance on the density of the branches and phase of the TiO_2.

Photocatalytic performances of TiO_2 nanobelts with different nanobranch array density were comparatively evaluated by measuring the degradation of MO aqueous solution under UV irradiation. Figure 7 shows degradation kinetics of the MO solution with addition of samples $^{400}HB_0$ −$^{400}HB_{0.4}$ and $^{550}HB_0$− $^{550}HB_{0.4}$, respectively. A series of digital photographs of MO color change under UV light irradiation for different times of all TiO_2 catalyst are shown in Supporting Information Figure S11. With the increase of time, gradually weakened yellow liquid can be observed, implying the decrease of MO concentration. The change in MO concentration as a function of UV irradiation time is represented in Figure 7a and b, which shows that without catalyst the concentration of MO does not change for every measurement. The difference between the

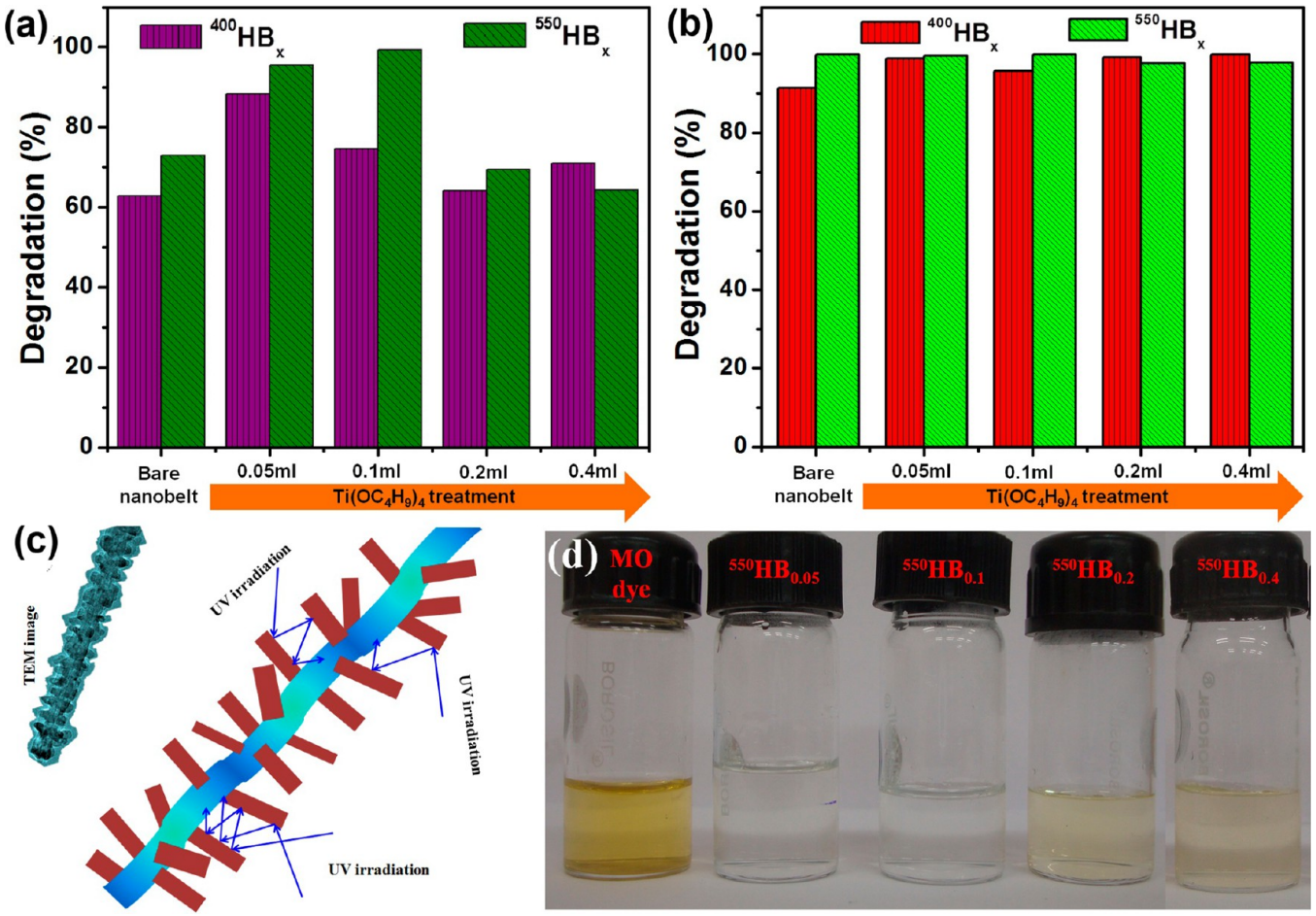

Figure 8. Bar diagram of the degradation percentages of $^{400}HB_x$ and $^{550}HB_x$: (a) after 30 min of illumination, and (b) after 60 min of illumination. (c) Schematic illustration of the UV light multireflections. (d) Digital photograph of the decolorization of MO for $^{550}HB_x$ after 30 min of UV exposure time.

initial absorption intensity at a certain reaction time and the residual intensity of the MO solution ($C_0 - C_t$) divided by the initial absorption intensity (C_0) represents the degree of degradation or decolorization percentages. The degradation percentages of all catalysts after 30 and 60 min irradiation are shown in Figure 8a and b. Figure 8a and b shows that the photocatalytic activity of the sample obtained at 550 °C is better than that of 400 °C. The photocatalytic performance of bare TiO_2 nanobelts is poor, and the MO degradation rate can only approach 63% for ^{400}HB and 73% for ^{550}HB after 30 min of UV light irradiation. In contrast, photocatalytic activity of the TiO_2 nanobelts with nanobranches is improved over this value, and the degree of MO degradation increases to 95.5% for $^{550}HB_{0.05}$ and 99.5% for $^{550}HB_{0.1}$ in 30 min under the same conditions. According to the XRD results (Figure 1 and Table 1), the crystallinity and the phase of the TiO_2 nanobelts play a key role in enhancement of the photocatalytic activity of the TiO_2 nanobelts. The catalytic activity of the sample obtained at 550 °C is significantly increased due to the higher crystallinity of the TiO_2 nanobelts. All of the mixed-phase nanobelt samples ($^{550}HB_x$) exhibited better photocatalytic activity than pure TiO_2(B) samples ($^{400}HB_x$); this fact suggests that the superior activity may originate from the interfaces between the TiO_2(B), anatase, and rutile phases. In addition, the photocatalytic performance of hierarchical nanostructure with different branch densities increases with density of the nanobranches (Figures 7 and 8). As shown in Figure 8, the degradation of MO after 30 min of illumination increases with increasing branch density; it increases to almost 100% and 95.5% for $^{550}HB_{0.1}$ and 95.5% for $^{550}HB_{0.1}$, respectively. At longer time (after 60 min), the degradation efficiency exhibited close to 100% for all samples. However, photocatalysis performance of the catalyst $^{550}HB_{0.4}$ obtained at 550 °C is lower (64%) than that of sample ($^{400}HB_{0.4}$) obtained at 400 °C (71%), due to the low branch density. In addition, as schematically illustrated in Figure 8 c, the branched hierarchical nanobelts can allow multiple reflections and scattering of UV light, which enhances light-harvesting and thus increases the quantity of photogenerated electrons and holes available to participate in the photocatalytic degradation of MO.[43,44] The dye color change sequence of all samples obtained at 550 °C after 30 min of UV illumination was visualized from the digital photograph (Figure 8d).

We compare the performance of catalyst with optimum branch density and bare nanobelt in Figure 9a and b, which clearly indicates that samples obtained at 550 °C with 0.1 mL of titanium butoxide treatment show best degradation activity, and $^{550}HB_{0.1}$ sample should have the ideal hierarchical structure. For comparison, degradation abilities of commercial P25 (Degussa Co. Ltd., Germany) were measured under the same experimental conditions. From Figure 9a, it was clear to conclude that the photodegradation rate of hierarchical nanobelt exhibited a significant improvement over P25. The

dx.doi.org/10.1021/am502379q | ACS Appl. Mater. Interfaces 2014, 6, 10044−10059

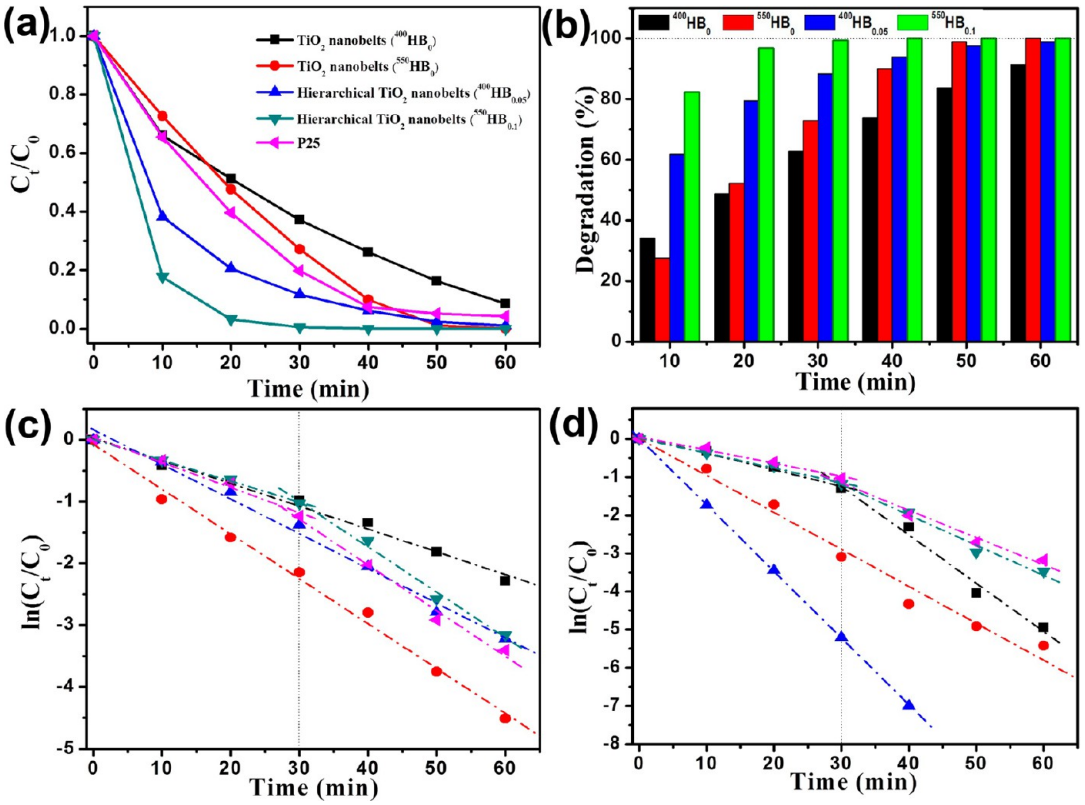

Figure 9. Comparison between bare nanobelt versus branched nanobelt: (a) degradation profiles, and (b) degradation percentages. (c,d) $\ln(C(t)/C_0)$ versus time (t) plot for determination of pseudo first-order rate constant.

Table 3. Performances of Photocatalytic Activity of TiO_2 Nanobelts in Previous Reported Literature

catalyst used and amount	concn and vol of MO	UV light source (W)	degradation time (min)	degradation %	ref
hierarchical	10^{-5} M	40	15	99.9	our work
nanobelts (20 mg)	40 mL				
N-doped TiO_2	20 mg/L	8	60	90	Wang et al.[15]
nanobelt (10 mg)	10 mL				
anatase TiO_2(101)	20 mg/L	148	60	98	Wu et al.[45]
nanobelt (10 mg)	10 mL				
TiO_2(B)/anatase	20 mg/L	300	50	99	Zhou et al.[46]
nanobelt (20 mg)	20 mL				
TiO_2(B)@anatase	5 mg/L	400	120	98	Zhang et al.[47]
nanobelt (20 mg)	20 mL				
Pt nanocrystals/titanate	10^{-4} M	125	300	99	Liu et al.[48]
nanobelts (50 mg)	50 mL				
NiO nanoparticle/TiO_2	20 mg/L	20	80	99	Lin et al.[49]
nanobelts (1 g/L)	20 mL				
Au nanocrystal/titanate	10^{-4} M	125	120	99.8	Liu[50]
nanobelts (50 mg)	50 mL				

observed photocatalytic performance of our synthesized branched nanobelts is far better as compared to most of the previous literature, which has been summarized in Table 3. The kinetic mechanism is important to describe the relationship between the initial degradation rate and the initial concentration. Here, the Langmuir–Hinshelwood (L–H) kinetic model was employed to describe the heterogeneous photocatalytic kinetic. In this work, experimental data were fitted to a pseudo first-order kinetic model, which is commonly represented by:[35,51]

$$C_t = C_0 \exp(-k_{app}t) \quad (12)$$

where k_{app} is the apparent reaction rate constant. Photocatalytic activity is quantified using the photodegradation rate coefficient (min^{-1}), which was determined from the slopes of $\ln(C(t)/C_0)$ versus t as shown in Figure 9c and d. Single stage decay was observed for samples $^{400}HB_0$, $^{400}HB_{0.05}$, $^{400}HB_{0.1}$, $^{550}HB_{0.05}$, and $^{550}HB_{0.1}$, but for the rest of the samples, linearity of the curves in two time stages indicates that the kinetics for the photocatalytic degradation follows a two-stage pseudo first-order rate. This two-stage kinetics was composed of an initial slow degradation stage (first stage; up to 30 min) followed by a rapid degradation stage (second stage; 30–60 min). Table 4 lists the decay rates constants as well as total percentages of

dx.doi.org/10.1021/am502379q | ACS Appl. Mater. Interfaces 2014, 6, 10044–10059

Table 4. Degradation Percentage and Pseudo First-Order Rate Constant

	degradation (%)		pseudo first-order rate constant	
sample	after 30 min	after 60 min	first stage	second stage
$^{400}HB_0$	63	91	0.03693	
$^{550}HB_0$	73	99.97	0.04338	0.12683
$^{400}HB_{0.05}$	88	98.9	0.07267	
$^{550}HB_{0.05}$	95.5	99.5	0.09704	
$^{400}HB_{0.1}$	74.7	95.6	0.05626	
$^{550}HB_{0.1}$	99.5	99.97	0.17474	
$^{400}HB_{0.2}$	64	99	0.03391	0.07348
$^{550}HB_{0.2}$	69.5	97.7	0.03901	0.07932
$^{400}HB_{0.4}$	71	99.97	0.04074	0.07396
$^{550}HB_{0.4}$	64	97.88	0.03469	0.07148

MO degradation after 30 and 60 min of reaction. The decay rate for $^{550}HB_{0.1}$ was obviously faster than that of the other.

The photocatalytic stability is very important for cycling use of the catalysts on the basis of its importance for long-term practical application. To investigate the photocatalytic stability of our samples in recycled process, 10 cycles of photodegradation of MO were conducted taking $^{550}HB_0$ and $^{550}HB_{0.1}$ catalyst as a typical sample. Figure 10 shows that there is no obvious reduction of the photocatalytic degradation efficiency after a successive 10 repeated cycles.

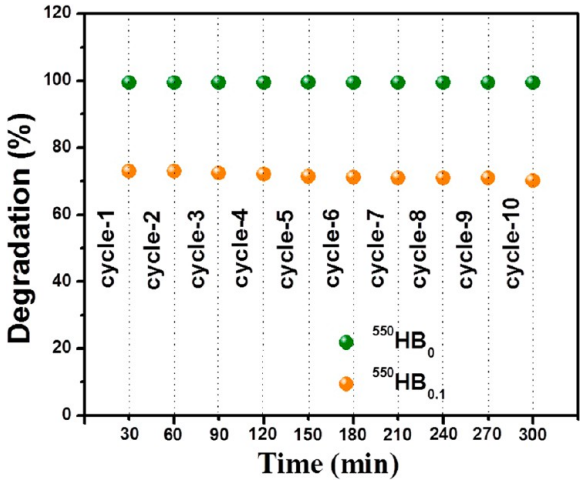

Figure 10. Cyclic MO degradation percentage for $^{550}HB_0$ and $^{550}HB_{0.1}$ photocatalyst.

To further confirm that interfaces between the mixed phases can improve the charge separation and suppress the recombination of excited carriers, luminescence decay measurements of the samples were recorded at 450 nm, as shown in Figure 11a–c. The decay profile was well-fitted by the biexponential function: $a_1 \cdot \exp(\tau/\tau_1) + a_2 \cdot \exp(\tau/\tau_2)$. The lifetimes and relative amplitudes of the fitting results are listed in Table 5 with two lifetime components τ_1 and τ_2. $^{550}HB_0$ and $^{550}HB_{0.1}$ exhibited much longer lifetime due to charge separation in the band edge, where excited electrons and holes trap prior to recombination.[52] This delay in recombination of charge species leads to higher photocatalytic activity by the photogenerated electron and holes for oxidation and reduction reaction. The interfacial surface to bulk defects at the TiO_2(B)/anatase/rutile junction significantly improve photocatalytic efficiency.[53] So the surface area is an important parameter for photocatalysis. The specific surface area, S_A, was calculated from the Brunauer–Emmett–Teller (BET) model[6,54] $S_A = 6/\rho d$, where d is the dimension of the catalyst (calculated from Figure 4 and Supporting Information Figure S7) and ρ is the density of the bulk TiO_2 (ρ = 3.9 g cm^{-3}). The specific surface area of the $^{400}HB_0$, $^{400}HB_{0.05}$, $^{550}HB_0$, and $^{550}HB_{0.1}$ was calculated to be 36.6, 38.4, 192.3, and 139.8 m^2/g, respectively. The above results obviously show that effective surface areas of hierarchical branched nanobelts were larger than the surface of bare TiO_2 nanobelt. Thus, the larger specific surface area of branched nanobelts will increase the photocatalytic reaction sites for the adsorption of reactant molecules and promote the efficiency of the electron–hole separation.

Mechanism of Photocatalytic Activity. To understand the photocatalytic degradation mechanism, potassium iodide (KI) and methanol were introduced to react with active species to evaluate their contributions on the photodegradation. For better information regarding the pathway of the photocatalytic reaction, the effect of KI and methanol on MO degradation in the presence of single phase TiO_2(B) catalyst was examined under the same conditions but two different experiments. One is the effect of methanol, known as hole (h^+) scavenger, for $^{400}HB_{0.1}$ and MO system, and the other is the effect of potassium iodide (I^-), known as the hydroxyl radicals, h^+ scavengers, for $^{400}HB_{0.05}$ and MO system.[55,56] As can be seen from Figure 11d, the photocatalytic degradation rate of MO is much higher without scavenger. When methanol is added, the degradation rates changed from 75% to 42%. Yet when excess KI is added, the degradation rates changed from 88% to 25%. This revealed that the photodegradation activity was suppressed when either I^- or methanol was added. The results suggest that the holes and hydroxyl radical pathways play a crucial role in the reaction mechanism.

Interfacial Electron Transfer and Proposed Mechanism. During the photocatalytic process, the presence of another semiconductor cocatalyst provides special active sites for the adsorption/reaction of reactants/reaction intermediates.[57] A second cocatalyst semiconductor can also modify the composite band structure, helping to change the bandgap absorption and to separate the photoexcited electron–hole pairs. In our work, we focus on the band bending effect among mixed-phase TiO_2 consisting of TiO_2(B), anatase, and rutile. The energy band structure of mixed-phase nanostructure can be determined by the values of band gap, valence band edge (VBE), and conduction band edge (CBE) position. Rutile has a 3.0 eV band gap, while that of both TiO_2(B) and anatase have 3.2 eV, but the VBE and CBE positions of these three polymorphs of TiO_2 are different.[58] The conductive band of anatase phase locates at a higher energy position than that of rutile phase by about 0.20 eV,[59] while the conductive band of anatase phase locates at a lower energy position than that of TiO_2(B).[60] When the three phases are in contact, there will be a difference between the band edges of the engaged phases. On the basis of the above energy band structure of three polymorphs, and scavenger test, a proposed schematic energy band structure of mixed phase is shown in Scheme 2. Under UV illumination, conduction band electrons (e_{CB}^-) and valence band holes (h_{VB}^+) are generated. The photogenerated holes from the valence band of rutile and anatase can pass through the interface and migrate to the valence band of the TiO_2(B) phase similarly; photoexcited electrons migrate from the higher

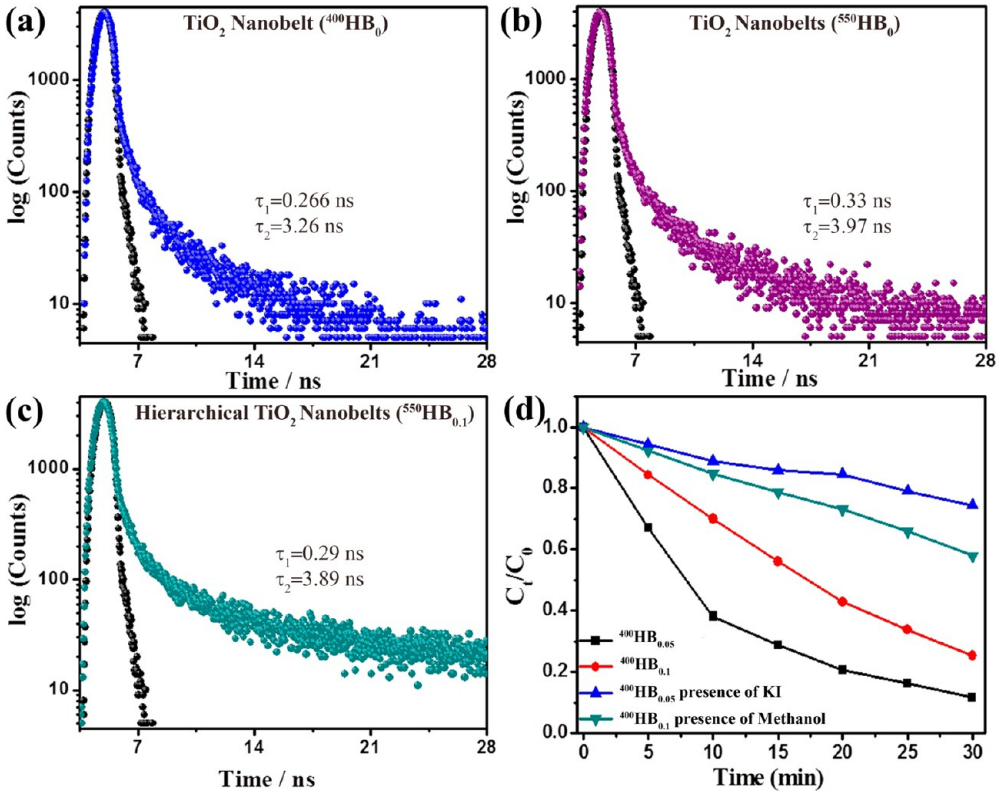

Figure 11. Typical fluorescence decay curves of (a) $^{400}HB_0$, (b) $^{550}HB_0$, (c) $^{550}HB_{0.1}$, and (d) comparison of the photocatalytic degradation of MO in the presence of various hole scavengers.

Table 5. Parameters of the Emission Decay of $^{400}HB_0$, $^{550}HB_0$, and $^{550}HB_{0.1}$

sample	a_1	τ_1	a_2	τ_2	τ_{av}
$^{400}HB_0$	0.90	0.10	0.266	3.26	0.56
$^{550}HB_0$	0.85	0.15	0.33	3.97	0.88
$^{550}HB_{0.1}$	0.85	0.15	0.29	3.89	0.83

conduction band of TiO_2(B) to the slightly lower conduction band of anatase. Now these conduction band electrons in anatase phase migrate to the lower conduction band of rutile. The overall outcome of the interphase charge migration is that the photogenerated electrons accumulate in the conduction band of rutile, and higher hole concentration is in the TiO_2(B) side. This process reduces the recombination of the photogenerated charges and consequently improves the photocatalytic efficiency. The photogenerated electrons react with adsorbed oxygen (air) and water molecules on the surface of the nanostructure and produce superoxide radical anions such as $\cdot O_2^-$OOH,OH^-,H_2O. The photogenerated holes can be trapped by H_2O and OH^- to further produce $\cdot$OH,OH^- species. These powerful superoxide radical as well as oxidizing agent ($\cdot O_2^-$,$\cdot$OH,$\cdot$OOH,OH^-) might be responsible for degradation of organic dyes.

CONCLUSIONS

Novel hierarchical branch TiO_2 nanobelts of length 30−50 μm and diameter in the range of 25−60 nm, with a high and

Scheme 2. Schematic Representation of Possible Electron−Hole Separation Mechanism Proposed for Mixed Phase Branch TiO_2 Nanobelt

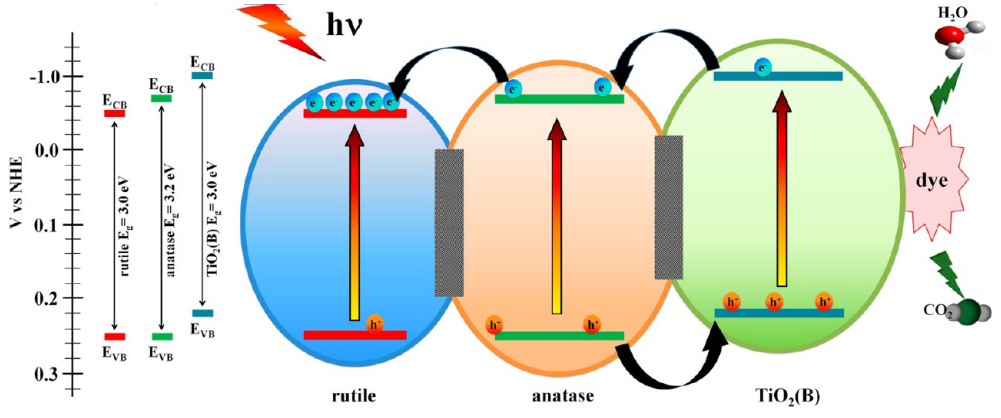

uniform branch density, have been successfully synthesized. The amount of titanium butoxide in chemical bath deposition decides the growth rate and densities of the nanobranches of length 15 nm and width about 8 nm, and therefore the branch density and phase of the nanostructure were controlled precisely to enhance the photocatalytic activity. Our findings show that photocatalytic activity exhibited by the TiO_2(B)/anatase/rutile mixed phase hierarchical branch nanobelts was superior to that of single phase and bare smooth TiO_2 nanobelts. In particular, $^{550}HB_{0.1}$ shows 99.5% degradation of MO in 30 min as compared to bare/pure nanobelt, which was only 63%. The enhanced activity was mainly due to the effective electron−hole separation at the interfaces among the band edges and multiple reflections and scattering of electromagnetic wave between the nanobranches. In addition to the removal of pollutants, these newly synthesized branch nanobelts can be used for applications in different fields, such as hydrogen generation through water splitting, lithium ion batteries, optoelectronic devices, sensors, solar cells, etc.

■ ASSOCIATED CONTENT

Supporting Information

XRD pattern of sodium titanate, hydrogen titanate nanobelts, and hierarchical nanobelts calcination at 700 °C. FESEM images of TiO_2 nanobelts at different hydrothermal reaction, HCl acid effect on the nanobelts, and ^{700}HB series. TEM images of single "branched nanobelt". EDS spectrum for all samples, magnified Raman spectrum. Digital photographs of the filtrate solution. Digital photographs of MO under UV light irradiation for different times. This material is available free of charge via the Internet at http://pubs.acs.org.

■ AUTHOR INFORMATION

Corresponding Author

*Fax: 91 33 24146007. E-mail: kalyan_chattopadhyay@yahoo.com.

Notes

The authors declare no competing financial interest.

■ ACKNOWLEDGMENTS

We wish to thank the University Grants Commission (UGC), the Government of India, for providing a research fellowship under "UGC-research fellowship in science for meritorious students" scheme during the execution of the work. We thank the DST and the UGC, the Government of India for the "University with potential for excellence (UPEII)" scheme.

■ REFERENCES

(1) Pan, Z. W.; Dai, Z. R.; Wang, Z. L. Nanobelts of Semiconducting Oxides. *Science* **2001**, *291*, 1947−1949.

(2) Huang, L. M.; Wang, H. T.; Wang, Z. B.; Mitra, A.; Bozhilov, K. N.; Yan, Y. S. Nanowire Arrays Electrodeposited from Liquid Crystalline Phases. *Adv. Mater.* **2002**, *14*, 61−64.

(3) Na, J.-S.; Gong, B.; Scarel, G.; Parsons, G. N. Surface Polarity Shielding and Hierarchical ZnO Nano-Architectures Produced Using Sequential Hydrothermal Crystal Synthesis and Thin Film Atomic Layer Deposition. *ACS Nano* **2009**, *3*, 3191−3199.

(4) Gao, Z.; Wu, Z.; Li, X.; Chang, J.; Wu, D.; Ma, P.; Xu, F.; Gao, S.; Jiang, K. Application of Hierarchical TiO2 Spheres as Scattering Layer for Enhanced Photovoltaic Performance in Dye Sensitized Solar Cell. *CrystEngComm* **2013**, *15*, 3351−3358.

(5) Liu, B.; Huang, Y.; Wen, Y.; Du, L.; Zeng, W.; Shi, Y.; Zhang, F.; Zhu, G.; Xu, X.; Wang, Y. Highly Dispersive {001} Facets-Exposed Nanocrystalline TiO2 on High Quality Graphene as a High Performance Photocatalyst. *J. Mater. Chem.* **2012**, *22*, 7484−7491.

(6) Sarkar, D.; Ghosh, C. K.; Mukherjee, S.; Chattopadhyay, K. K. Three Dimensional Ag2O/TiO2 Type-II (p−n) Nanoheterojunctions for Superior Photocatalytic Activity. *ACS Appl. Mater. Interfaces* **2012**, *5*, 331−337.

(7) Kim, T. W.; Ha, H.-W.; Paek, M.-J.; Hyun, S.-H.; Choy, J.-H.; Hwang, S.-J. Unique Phase Transformation Behavior and Visible Light Photocatalytic Activity of Titanium Oxide Hybridized with Copper Oxide. *J. Mater. Chem.* **2010**, *20*, 3238−3245.

(8) Yang, D.; Zhao, J.; Liu, H.; Zheng, Z.; Adebajo, M. O.; Wang, H.; Liu, X.; Zhang, H.; Zhao, J.-c.; Bell, J.; Zhu, H. Enhancing Photoactivity of TiO2(B)/Anatase Core−Shell Nanofibers by Selectively Doping Cerium Ions into the TiO2(B) Core. *Chem.—Eur. J.* **2013**, *19*, 5113−5119.

(9) He, Z.; Que, W.; Chen, J.; Yin, X.; He, Y.; Ren, J. Photocatalytic Degradation of Methyl Orange over Nitrogen−Fluorine Codoped TiO2 Nanobelts Prepared by Solvothermal Synthesis. *ACS Appl. Mater. Interfaces* **2012**, *4*, 6816−6826.

(10) Sarkar, D.; Ghosh, C. K.; Chattopadhyay, K. K. Morphology Control of Rutile TiO2 Hierarchical Architectures and their Excellent Field Emission Properties. *CrystEngComm* **2012**, *14*, 2683−2690.

(11) Liao, J.-Y.; Higgins, D.; Lui, G.; Chabot, V.; Xiao, X.; Chen, Z. Multifunctional TiO2−C/MnO2 Core−Double-Shell Nanowire Arrays as High-Performance 3D Electrodes for Lithium Ion Batteries. *Nano Lett.* **2013**, *13*, 5467−5473.

(12) Tao, L.; Xiong, Y.; Liu, H.; Shen, W. High performance PbS Quantum Dot Sensitized Solar Cells via Electric Field Assisted in Situ Chemical Deposition on Modulated TiO2 Nanotube Arrays. *Nanoscale* **2014**, *6*, 931−938.

(13) Zhang, H.; Li, G. R.; An, L. P.; Yan, T. Y.; Gao, X. P.; Zhu, H. Y. Electrochemical Lithium Storage of Titanate and Titania Nanotubes and Nanorods. *J. Phys. Chem. C* **2007**, *111*, 6143−6148.

(14) Chen, X.; Mao, S. S. Titanium Dioxide Nanomaterials: Synthesis, Properties, Modifications, and Applications. *Chem. Rev.* **2007**, *107*, 2891−2959.

(15) Wang, J.; Tafen, D. N.; Lewis, J. P.; Hong, Z.; Manivannan, A.; Zhi, M.; Li, M.; Wu, N. Origin of Photocatalytic Activity of Nitrogen-Doped TiO2 Nanobelts. *J. Am. Chem. Soc.* **2009**, *131*, 12290−12297.

(16) Li, G.-R.; Zheng, F.-L.; Tong, Y.-X. Controllable Synthesis of Bi2Te3 Intermetallic Compounds with Hierarchical Nanostructures via Electrochemical Deposition Route. *Cryst. Growth Des.* **2008**, *8*, 1226−1232.

(17) Xiao, H.; Ai, Z.; Zhang, L. Nonaqueous Sol−Gel Synthesized Hierarchical CeO2 Nanocrystal Microspheres as Novel Adsorbents for Wastewater Treatment. *J. Phys. Chem. C* **2009**, *113*, 16625−16630.

(18) Ostermann, R.; Li, D.; Yin, Y.; McCann, J. T.; Xia, Y. V2O5 Nanorods on TiO2 Nanofibers: A New Class of Hierarchical Nanostructures Enabled by Electrospinning and Calcination. *Nano Lett.* **2006**, *6*, 1297−1302.

(19) Ko, S. H.; Lee, D.; Kang, H. W.; Nam, K. H.; Yeo, J. Y.; Hong, S. J.; Grigoropoulos, C. P.; Sung, H. J. Nanoforest of Hydrothermally Grown Hierarchical ZnO Nanowires for a High Efficiency Dye-Sensitized Solar Cell. *Nano Lett.* **2011**, *11*, 666−671.

(20) Kwon, K.-W.; Shim, M. γ-Fe2O3/II−VI Sulfide Nanocrystal Heterojunctions. *J. Am. Chem. Soc.* **2005**, *127*, 10269−10275.

(21) Ohgi, H.; Maeda, T.; Hosono, E.; Fujihara, S.; Imai, H. Evolution of Nanoscale SnO2 Grains, Flakes, and Plates into Versatile Particles and Films through Crystal Growth in Aqueous Solutions. *Cryst. Growth Des.* **2005**, *5*, 1079−1083.

(22) Ding, Y. S.; Shen, X. F.; Gomez, S.; Luo, H.; Aindow, M.; Suib, S. L. Hydrothermal Growth of Manganese Dioxide into Three-Dimensional Hierarchical Nanoarchitectures. *Adv. Funct. Mater.* **2006**, *16*, 549−555.

(23) Zhang, T.; Dong, W.; Keeter-Brewer, M.; Konar, S.; Njabon, R. N.; Tian, Z. R. Site-Specific Nucleation and Growth Kinetics in Hierarchical Nanosyntheses of Branched ZnO Crystallites. *J. Am. Chem. Soc.* **2006**, *128*, 10960−10968.

(24) Li, R.; Sun, X.; Zhou, X.; Cai, M.; Sun, X. Aligned Heterostructures of Single-Crystalline Tin Nanowires Encapsulated in Amorphous Carbon Nanotubes. *J. Phys. Chem. C* **2007**, *111*, 9130−9135.
(25) Sun, C.; Wang, N.; Zhou, S.; Hu, X.; Zhou, S.; Chen, P. Preparation of Self-Supporting Hierarchical Nanostructured Anatase/Rutile Composite TiO2 Film. *Chem. Commun.* **2008**, *0*, 3293−3295.
(26) McDaniel, H.; Shim, M. Size and Growth Rate Dependent Structural Diversification of Fe3O4/CdS Anisotropic Nanocrystal Heterostructures. *ACS Nano* **2009**, *3*, 434−440.
(27) Devika, M.; Koteeswara Reddy, N.; Pevzner, A.; Patolsky, F. Heteroepitaxial Si/ZnO Hierarchical Nanostructures for Future Optoelectronic Devices. *ChemPhysChem* **2010**, *11*, 809−814.
(28) Buonsanti, R.; Grillo, V.; Carlino, E.; Giannini, C.; Gozzo, F.; Garcia-Hernandez, M.; Garcia, M. A.; Cingolani, R.; Cozzoli, P. D. Architectural Control of Seeded-Grown Magnetic−Semicondutor Iron Oxide−TiO2 Nanorod Heterostructures: The Role of Seeds in Topology Selection. *J. Am. Chem. Soc.* **2010**, *132*, 2437−2464.
(29) Sarkar, D.; Maiti, U. N.; Ghosh, C. K.; Chattopadhyay, K. K. Excellent Photocatalytic Activity of Mixed Phase Ultra Slim TiO2 Nanofibers for the Degradation of Organic Wastes. *Adv. Sci. Lett.* **2012**, *6*, 127−133.
(30) Wen, B.-M.; Liu, C.-Y.; Liu, Y. Solvothermal synthesis of ultralong single-crystalline TiO2 nanowires. *New J. Chem.* **2005**, *29*, 969−971.
(31) Yang, D.; Liu, H.; Zheng, Z.; Yuan, Y.; Zhao, J.-C.; Waclawik, E. R.; Ke, X.; Zhu, H. An Efficient Photocatalyst Structure: TiO2(B) Nanofibers with a Shell of Anatase Nanocrystals. *J. Am. Chem. Soc.* **2009**, *131*, 17885−17893.
(32) Li, J.; Wan, W.; Zhou, H.; Li, J.; Xu, D. Hydrothermal Synthesis of TiO2(B) Nanowires with Ultrahigh Surface Area and their Fast Charging and Discharging Properties in Li-ion Batteries. *Chem. Commun.* **2011**, *47*, 3439−3441.
(33) Yang, Z.; Du, G.; Guo, Z.; Yu, X.; Chen, Z.; Guo, T.; Zeng, R. Encapsulation of TiO2(B) Nanowire Cores into SnO2/Carbon Nanoparticle Shells and their High Performance in Lithium Storage. *Nanoscale* **2011**, *3*, 4440−4447.
(34) Pan, X.; Zhao, Y.; Liu, S.; Korzeniewski, C. L.; Wang, S.; Fan, Z. Comparing Graphene-TiO2 Nanowire and Graphene-TiO2 Nanoparticle Composite Photocatalysts. *ACS Appl. Mater. Interfaces* **2012**, *4*, 3944−3950.
(35) Sarkar, D.; Mukherjee, S.; Chattopadhyay, K. K. Synthesis, Characterization and High Natural Sunlight Photocatalytic Performance of Cobalt Doped TiO2 Nanofibers. *Phys. E (Amsterdam, Neth.)* **2013**, *50*, 37−43.
(36) Pan, K.; Dong, Y.; Tian, C.; Zhou, W.; Tian, G.; Zhao, B.; Fu, H. TiO2-B Narrow Nanobelt/TiO2 Nanoparticle Composite Photoelectrode for Dye-Sensitized Solar Cells. *Electrochim. Acta* **2009**, *54*, 7350−7356.
(37) Dylla, A. G.; Lee, J. A.; Stevenson, K. J. Influence of Mesoporosity on Lithium-Ion Storage Capacity and Rate Performance of Nanostructured TiO2(B). *Langmuir* **2012**, *28*, 2897−2903.
(38) Wang, F.; Liu, Y.; Dong, W.; Shen, M.; Kang, Z. Tuning TiO2 Photoelectrochemical Properties by Nanoring/Nanotube Combined Structure. *J. Phys. Chem. C* **2011**, *115*, 14635−14640.
(39) Ben Yahia, M.; Lemoigno, F.; Beuvier, T.; Filhol, J. S.; Richard-Plouet, M.; Brohan, L.; Doublet, M. L. Updated References for the Structural, Electronic, and Vibrational Properties of TiO2 (B) Bulk using First-Principles Density Functional Theory Calculations. *J. Chem. Phys.* **2009**, *130*, 204501.
(40) Erdemir, D.; Lee, A. Y.; Myerson, A. S. Nucleation of Crystals from Solution: Classical and Two-Step Models. *Acc. Chem. Res.* **2009**, *42*, 621−629.
(41) Park, J.; Joo, J.; Kwon, S. G.; Jang, Y.; Hyeon, T. Synthesis of Monodisperse Spherical Nanocrystals. *Angew. Chem., Int. Ed.* **2007**, *46*, 4630−4660.
(42) Kobayashi, H.; Lim, B.; Wang, J.; Camargo, P. H. C.; Yu, T.; Kim, M. J.; Xia, Y. Seed-Mediated Synthesis of Pd−Rh Bimetallic Nanodendrites. *Chem. Phys. Lett.* **2010**, *494*, 249−254.
(43) Wang, X.; Liao, M.; Zhong, Y.; Zheng, J. Y.; Tian, W.; Zhai, T.; Zhi, C.; Ma, Y.; Yao, J.; Bando, Y.; Golberg, D. ZnO Hollow Spheres with Double-Yolk Egg Structure for High-Performance Photocatalysts and Photodetectors. *Adv. Mater.* **2012**, *24*, 3421−3425.
(44) Zou, R.; He, G.; Xu, K.; Liu, Q.; Zhang, Z.; Hu, J. ZnO Nanorods on Reduced Graphene Sheets with Excellent Field Emission, Gas Sensor and Photocatalytic Properties. *J. Mater. Chem. A* **2013**, *1*, 8445−8452.
(45) Wu, N.; Wang, J.; Tafen, D. N.; Wang, H.; Zheng, J.-G.; Lewis, J. P.; Liu, X.; Leonard, S. S.; Manivannan, A. Shape-Enhanced Photocatalytic Activity of Single-Crystalline Anatase TiO2 (101) Nanobelts. *J. Am. Chem. Soc.* **2010**, *132*, 6679−6685.
(46) Zhou, W.; Gai, L.; Hu, P.; Cui, J.; Liu, X.; Wang, D.; Li, G.; Jiang, H.; Liu, D.; Liu, H.; Wang, J. Phase Transformation of TiO2 Nanobelts and TiO2(B)/Anatase Interface Heterostructure Nanobelts with Enhanced Photocatalytic Activity. *CrystEngComm* **2011**, *13*, 6643−6649.
(47) Zhang, Y.; Xu, J.; Feng, J.; Yang, A.; Liu, Y.; Zhi, M.; Hong, Z. Enhanced Photocatalytic Degradation of Methyl Orange in TiO2(B)@Anatase Heterostructure Nanocomposites Prepared by a Facile Hydrothermal Method. *Mater. Lett.* **2013**, *112*, 173−176.
(48) Liu, Y.; Zhong, L.; Peng, Z.; Cai, Y.; Song, Y.; Chen, W. Self-Assembly of Pt Nanocrystals/One-Dimensional Titanate Nanobelts Heterojunctions and their Great Enhancement of Photocatalytic Activities. *CrystEngComm* **2011**, *13*, 5467−5473.
(49) Lin, J.; Shen, J.; Wang, R.; Cui, J.; Zhou, W.; Hu, P.; Liu, D.; Liu, H.; Wang, J.; Boughton, R. I.; Yue, Y. Nano-p-n Junctions on Surface-Coarsened TiO2 Nanobelts with Enhanced Photocatalytic Activity. *J. Mater. Chem.* **2011**, *21*, 5106−5113.
(50) Liu, Y.; Shu, W.; Peng, Z.; Chen, K.; Chen, W. Self-Assembly of Au Nanocrystal/Titanate Nanobelt Heterojunctions and Enhancement of the Photocatalytic Activity. *Catal. Today* **2013**, *208*, 28−34.
(51) An, C.; Jiang, W.; Wang, J.; Wang, S.; Ma, Z.; Li, Y. Synthesis of Three-Dimensional AgI@TiO2 Nanoparticles with Improved Photocatalytic Performance. *Dalton Trans.* **2013**, *42*, 8796−8801.
(52) Ren, L.; Tian, T.; Li, Y.; Huang, J.; Zhao, X. High-Performance UV Photodetection of Unique ZnO Nanowires from Zinc Carbonate Hydroxide Nanobelts. *ACS Appl. Mater. Interfaces* **2013**, *5*, 5861−5867.
(53) Kong, M.; Li, Y.; Chen, X.; Tian, T.; Fang, P.; Zheng, F.; Zhao, X. Tuning the Relative Concentration Ratio of Bulk Defects to Surface Defects in TiO2 Nanocrystals Leads to High Photocatalytic Efficiency. *J. Am. Chem. Soc.* **2011**, *133*, 16414−16417.
(54) Fielding, L. A.; Mykhaylyk, O. O.; Armes, S. P.; Fowler, P. W.; Mittal, V.; Fitzpatrick, S. Correcting for a Density Distribution: Particle Size Analysis of Core−Shell Nanocomposite Particles Using Disk Centrifuge Photosedimentometry. *Langmuir* **2012**, *28*, 2536−2544.
(55) Mohamed, H. H.; Mendive, C. B.; Dillert, R.; Bahnemann, D. W. Kinetic and Mechanistic Investigations of Multielectron Transfer Reactions Induced by Stored Electrons in TiO2 Nanoparticles: A Stopped Flow Study. *J. Phys. Chem. A* **2011**, *115*, 2139−2147.
(56) He, Z.; Wang, C.; Wang, H.; Hong, F.; Xu, X.; Chen, J.; Song, S. Increasing the Catalytic Activities of Iodine Doped Titanium Dioxide by Modifying with Tin Dioxide for the Photodegradation of 2-chlorophenol under Visible Light Irradiation. *J. Hazard. Mater.* **2011**, *189*, 595−602.
(57) Zhang, Z.; Yates, J. T. Band Bending in Semiconductors: Chemical and Physical Consequences at Surfaces and Interfaces. *Chem. Rev.* **2012**, *112*, 5520−5551.
(58) Hoang, S.; Berglund, S. P.; Hahn, N. T.; Bard, A. J.; Mullins, C. B. Enhancing Visible Light Photo-oxidation of Water with TiO2 Nanowire Arrays via Cotreatment with H2 and NH3: Synergistic Effects between Ti3+ and N. *J. Am. Chem. Soc.* **2012**, *134*, 3659−3662.
(59) Li, G.-L.; Li, W.-X.; Li, C. Model Relation between the Energy-Band Edge and the Fermi Level of the Nondegenerate Semiconductor TiO_{2}: Application to Electrochemistry. *Phys. Rev. B* **2010**, *82*, 235109.

(60) Bai, Y.; Li, W.; Liu, C.; Yang, Z.; Feng, X.; Lu, X.; Chan, K.-Y. Stability of Pt Nanoparticles and Enhanced Photocatalytic Performance in Mesoporous Pt-(Anatase/TiO2(B)) Nanoarchitecture. *J. Mater. Chem.* **2009**, *19*, 7055−7061.